doi:10.26443/seismica.v5i1.2027

The normal stress dependence of rock friction

Sylvain Barbot * [1]

[1]Department of Earth Sciences, University of Southern California, Los Angeles, USA

Author contributions: *Conceptualization, Methodology, Formal Analysis, Original draft, Investigation, Visualization*: S. Barbot.

Abstract Rock friction governs lithospheric strength and earthquake mechanics, yet its fundamental characteristics remain poorly understood. A survey of experimental data on the frictional resistance of bare contacts or powdered gouge from 41 published studies encompassing 119 rocks and synthetic materials reveals a power-law dependence between sliding friction and effective normal stress from 10 Pa to 1 GPa. For framework silicates, ice, and most synthetic materials considered, the friction coefficient is a decreasing function of effective normal stress, in contrast with water-saturated phyllosilicates. The normal stress dependence of the friction coefficient is controlled by the real area of contact, possibly modulated by osmotic pressure near contact junctions for phyllosilicates. Cohesion is negligible at macroscopic scales for fractures with rough contacts. These experimental findings challenge the conventional representation of rock friction as a linear function of normal stress. These results provide critical constraints for advancing physical models of rock friction and fault mechanics.

Production Editor: Yen Joe Tan, Christie D. Rowe
Handling Editor: Ake Fagereng
Copy & Layout Editor: Miguel Neves

Received: September 22, 2025
Accepted: February 9, 2026
Published: February 26, 2026

Résumé Le frottement des roches contrôle la résistance lithosphérique et la mécanique des séismes, mais ses caractéristiques fondamentales restent mal comprises. Une analyse des données expérimentales issues de 41 articles à comité de lecture, portant sur 119 roches et matériaux synthétiques, révèle une dépendance en loi de puissance entre la résistance et la contrainte normale effective, de 10 Pa à 1 GPa. Pour les silicates à structure tridimensionnelle, la glace et la plupart des matériaux synthétiques étudiés, le coefficient de frottement diminue avec la contrainte normale effective, contrairement aux phyllosilicates saturés en eau. La dépendance du coefficient de frottement à la contrainte normale est contrôlée par la surface réelle de contact, potentiellement modulée par la pression osmotique près des zones de contact pour les phyllosilicates. La cohésion est négligeable aux échelles macroscopiques pour les fractures avec des contacts rugueux. Ces résultats expérimentaux remettent en cause la représentation conventionnelle du frottement des roches comme une fonction linéaire de la contrainte normale. Ces résultats fournissent des contraintes essentielles pour faire progresser les modèles physiques du frottement des roches et de la mécanique des tremblements de terre.

Non-technical summary As rock friction plays an important role in the mechanics of earthquakes and plate tectonics, it has been the subject of intense scientific investigation. Classical models describe the frictional resistance of rocks involving cohesion and a linear increase with normal stress. This description is inaccurate. By reviewing a large body of experimental measurements on rocks and synthetic materials, I show that the rock friction is characterized by a power-law relationship with normal stress. Frictional strength is proportional to the normal stress raised to a power close to unity. As a result, the friction coefficient, defined as the ratio of shear stress to normal stress during sliding, also depends on normal stress. Whereas the friction coefficient is a decreasing function of normal stress for most rocks, it increases with normal stress for water-rich minerals like clay. These observations build a foundation for more accurate models of earthquakes and fault behavior.

Highlights

- Extensive review of experimental constraints on sliding friction for 119 materials.
- Rock friction follows a power-law of effective normal stress.
- The sensitivity of the friction coefficient on normal stress is different on water-saturated phyllosilicates.

1 Introduction

The dynamics of earthquakes is governed by the frictional behavior of rocks, which features complex dependencies on mineralogy, slip-rate, temperature, pressure, and fluid content (Horn and Deere, 1962; Noda and Shimamoto, 2009; Zhang and He, 2016; Niemeijer et al., 2016; Bedford et al., 2021; Okuda et al., 2022). Rock friction exhibits intricate feedbacks throughout the seismic cycle involving different physical processes during nucleation and rupture propagation. During nucleation, thermal or frictional instabilities interact with dilatancy effects (Segall and Rice, 1995; Rice, 2006; Beeler et al., 2008; Wang and Barbot, 2020). Seismic slip-rates

*Corresponding author: sbarbot@usc.edu

generate significant shear heating, potentially triggering pressurization of pore fluids (Noda and Lapusta, 2010; Viesca and Garagash, 2015), melting of the host rocks (Di Toro et al., 2006), and various thermally activated chemical reactions (Sulem and Famin, 2009; Takahashi et al., 2009; Okamoto et al., 2019). Disentangling these coupled processes is key to advancing earthquake science.

Among the key thermo-mechanical properties, the coefficient of kinetic friction, defined as the ratio of shear stress to effective normal stress during sliding on a pre-existing fracture, accounting for the effect of pore-fluid pressure, represents one of the most fundamental yet poorly understood characteristics. Prevailing models often assume a linear relationship between frictional resistance and effective normal stress, invoking cohesion at vanishing normal stress. However, this approximation is inaccurate and misleading. Although some studies acknowledge the nonlinear nature of rock friction through piecewise linear approximations (Byerlee, 1978), the underlying physics remains inadequately constrained. In this study, I present a systematic review of experimental rock friction data to elucidate its dependency on effective normal stress. The curated dataset spans 41 peer-reviewed studies, encompassing 119 natural and synthetic materials, including historical experiments on wood by Coulomb (1821), the extensive laboratory data on sedimentary and igneous rocks discussed by Byerlee (1978), and the experiments conducted in the last four decades on synthetic and natural samples, including water ice. Collectively, the experimental dataset covers effective normal stress from 10 Pa to 1 GPa and a wide range of lithology, including gouge-bearing and bare contacts.

I show that the linear model offers a useful approximation for experimental data covering a narrow range of effective normal stress, but leads to systematic residuals when a wider range of loads are considered. The linear model also incorrectly predicts negative strength for phyllosilicate-rich rocks at sufficiently low effective normal stress in water-saturated conditions. In contrast, a power-law relationship consistently describes the observed shear resistance across all materials, consistently explaining the frictional behavior of framework silicates, dry and water-saturated phyllosilicates, water ice, and engineered surfaces. Notably, cohesion becomes negligible at macroscopic scales where fault roughness dominates, as a great number of microasperities bear the shear and normal loads. The nonlinear dependency of rock friction is well understood conceptually, inheriting from the evolution of the real area of contact under normal load and the normal-stress dependence of the healing process. These findings invalidate the conventional linear approximation and provide critical constraints for physical models of rock friction.

2 Experimental constraints

I consider an extensive friction experimental dataset consisting of peer-reviewed studies on natural and synthetic materials. To the best of my knowledge, I include all high-quality experiments documenting the frictional resistance during sliding as a function of effective normal stress for at least three different normal loads. Motivated by the study of mature faults that are readily considerably fractured, I focus on sliding friction on pre-existing fractures and I exclude experimental work on intact samples (Figure 1, inset).

I include the dataset considered in the seminal work of Byerlee (1978), including experiments on Westerly granite, Spruce Pine dunite, Solenhofen sandstone, Oak Hall limestone, and Cabramurra serpentinite (Byerlee, 1968), sandstone, trachyte, Wombeyan marble (Hoskins et al., 1968), Blair dolomite, Solenhofen limestone, Know dolomite, and Tennessee limestone (Handin, 1969), Ormonde siltstone, Bulsthorpe silty mudstone, Hucknall shale, Bulsthorpe mudstone (Hobbs, 1970; Barton, 1973), Darley Dale sandstone (Murrell, 1965), and Weber sandstone (Barton, 1976).

I extend the dataset with the experiments conducted in the last four decades, primarily on natural fault gouge, synthetic gouge, and engineered surfaces. I consider the experiments on mixtures of smectite and quartz (Saffer and Marone, 2003), mixtures of montmorillonite and quartz (Ikari et al., 2007), mixtures of talc and calcite (Giorgetti et al., 2015), and mixtures of Opalinus clay with Berea sandstone (Rast et al., 2024). Experimental work on natural samples include Mt McRae shale (Lilly, 1982), illite shale (Saffer and Marone, 2003), sandstone and micaschist (Maksimović, 1992), fault gouge and schist from the Zuccale fault, Italy (Smith and Faulkner, 2010), natural cataclasites from the Moonlight fault zone, New Zealand (Smith et al., 2017), argillite, cataclasite, talc schist, and serpentinite from the Franciscan Complex, California (Hirauchi et al., 2020b), terrigenous sediment from the Costa Rica subduction zone (Kurzawski et al., 2018), antigorite, lizardite, and chrysotile serpentinites from the Ligurian ophiolite outcrop in Elba Island, Italy (Tesei et al., 2018), sediment from the C0008 borehole into the Nankai accretionary prism (Bedford et al., 2021), and fault gouge from the Atacama fault system, Chile (González et al., 2024).

Other experiments focus on specific minerals, including Ottawa sand (98% spherical quartz grains) and crushed quartzite (angular quartz gouge) (Morrow and Byerlee, 1989), powdered Carrara marble (>98% $CaCO_3$) (Carpenter et al., 2016), onyx marble (Mehrishal et al., 2016), halite (Hirauchi et al., 2020a; Chang et al., 2024), gypsum (Mutlu and Bobet, 2006), Opalinus clay (Orellana et al., 2018; Bigaroni et al., 2022), water-saturated montmorillonite (Morrow et al., 2017), dry mica (Sakuma et al., 2018), muscovite, montmorillonite, talc, and biotite (Moore and Lockner, 2008), and chrysotile serpentinite (Moore et al., 2004). I also include friction experiments on water ice at various temperatures (Beeman et al., 1988; Mizukami and Maeno, 2000; Schulson and Fortt, 2012). The experimental setup for the above studies includes double-direct shear, rotary shear, and triaxial deformation. Finally, I include the frictional properties of engineered surfaces made of glass microspheres (Schellart, 2000; Yashima et al., 2015; Maegawa et al., 2015), finely sorted caster sugar and sand (Schellart, 2000), plaster (Jaeger, 1959; Jang

Rock	Normal stress	Reference
Siltstone, mudstone, shale	0.5–60 MPa	Barton (1973)
Weber sandstone	30–320 MPa	Barton (1976)
Nankai accretionary prism	10–75 MPa	Bedford et al. (2021)
Water ice	0.1–2 MPa	Beeman et al. (1988)
Granite, gabbro, dunite, sandstone, limestone	15–650 MPa	Byerlee (1968)
Central California outcrops	4–100 MPa	Carpenter et al. (2009)
Calcite	1–100 MPa	Carpenter et al. (2016)
Halite	0.2–1 MPa	Chang et al. (2024)
Gouge from the Atacama Fault system, Chile	25–125 MPa	González et al. (2024)
Mixtures of talc and calcite	5–50 MPa	Giorgetti et al. (2015)
Limestone, dolomite	50–620 MPa	Handin (1969)
Argillite, cataclasite, talc schist, serpentinite	60–180 MPa	Hirauchi et al. (2020b)
Halite	8–113 MPa	Hirauchi et al. (2020a)
Sandstone, marble, trachyte	1–5 MPa	Hoskins et al. (1968)
Mixture of montmorillonite and quartz	5–100 MPa	Ikari et al. (2007)
Terrigenous clay sediments	30–110 MPa	Kurzawski et al. (2018)
Mt McRae shale	0.2–1.2 MPa	Lilly (1982)
Sandstone, micaschist	0.1–10 MPa	Maksimović (1992)
Onyx marble	2–50 MPa	Mehrishal et al. (2016)
Water ice	1–20 kPa	Mizukami and Maeno (2000)
Chrysotile serpentine at high-temperature	45–200 MPa	Moore et al. (2004)
Muscovite, montmorillonite, talc, mica	1–310 MPa	Moore and Lockner (2008)
Water-saturated montmorillonite	10–600 MPa	Morrow et al. (2017)
Ottawa sand, quartzite, Westerly granite	12.5–100 MPa	Morrow and Byerlee (1989)
Darley Dale sandstone	10–400 MPa	Murrell (1965)
Gypsum	0.1–3 MPa	Mutlu and Bobet (2006)
Opalinus clay	4–30 MPa	Orellana et al. (2018)
Opalinus clay & Berea sandstone mixture	5–35 MPa	Rast et al. (2024)
Quartz, illite shale, mixture of smectite and quartz	5–150 MPa	Saffer and Marone (2003)
Dry mica	5–60 MPa	Sakuma et al. (2018)
Water ice	20–100 kPa	Schulson and Fortt (2012)
Fault gouge, schist	25–75 MPa	Smith and Faulkner (2010)
Cataclasites	5–75 MPa	Smith et al. (2017)
Antigorite, lizardite, chrysotile serpentinites	5–100 MPa	Tesei et al. (2018)

Synthetic material	Normal stress	Reference
Oak wood, pine wood, elm wood	1–300 kPa	Coulomb (1821)
Commercial plaster	7–230 MPa	Jaeger (1959)
GM-10, Gemstone N-2000, Diestone plasters	0.2–3.4 MPa	Jang and Jang (2014)
PDMS glass	1–6 kPa	Maegawa et al. (2015)
Caster sugar, sand, glass microsphere	50–500 Pa	Schellart (2000)
Pozzolanic mortar	5–40 MPa	Volpe et al. (2025)
Pozzolanic mortar	0.5–80 MPa	Volpe et al. (2026)
Glass small microsphere	1–2 kPa	Yashima et al. (2015)

Table 1 Experimental data considered in the study, encompassing 119 different rocks and synthetic materials.

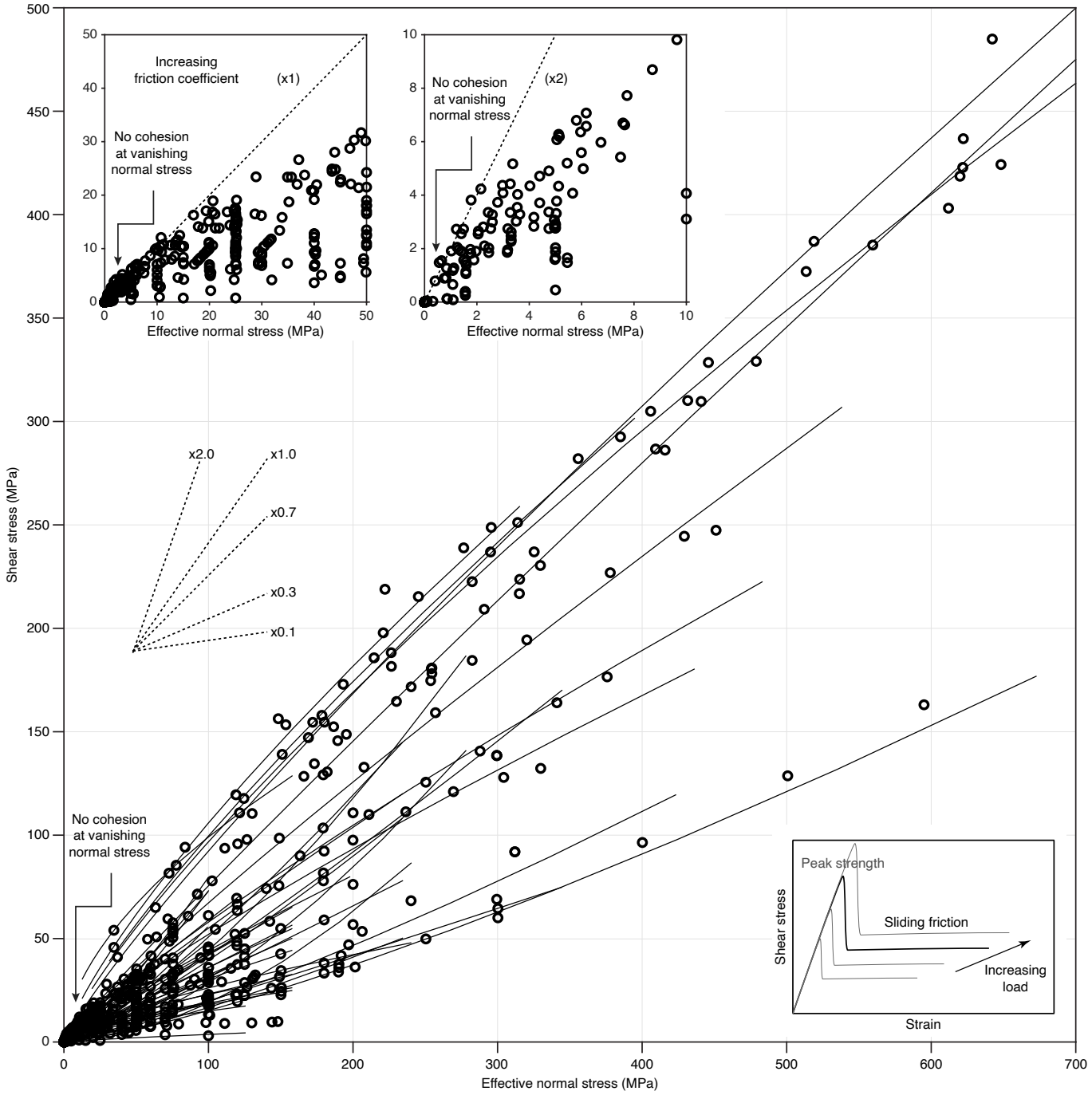

Figure 1 Rock sliding friction from the experimental studies listed in Table 1, including natural and synthetic gouge, ice, and engineered materials. The top insets show the same data for a smaller range of effective normal stress, highlighting the normal stress dependence of the friction coefficient. The thin lines correspond to the least-squares best-fitting power-law model for the corresponding dataset based on Equation (1). The dashed lines indicate a linear relationship for a given proportionality coefficient. The bottom inset show a schematic of typical rock strength (e.g., Byerlee, 1968), highlighting the domain of sliding friction discussed in this study.

and Jang, 2014), dry and wet mortar (Volpe et al., 2025, 2026), and the historical experiments of Coulomb (1821) on oak, pine, and elm wood.

In total, the curated dataset includes 119 different materials in various ranges of normal stress, as summarized in Table 1. Some 19 datasets contain strength measurements at only 3 different normal loads. However, more than 32 datasets contain 10 to 20 different measurements (Murrell, 1965; Byerlee, 1968; Barton, 1976; Lilly, 1982; Mizukami and Maeno, 2000; Saffer and Marone, 2003; Moore et al., 2004; Mutlu and Bobet, 2006; Moore and Lockner, 2008; Yashima et al., 2015; Morrow et al., 2017; Sakuma et al., 2018; Tesei et al., 2018; Kurzawski et al., 2018; Rast et al., 2024). Some 16 datasets contain between 20 and 30 measurements (Jaeger, 1959; Barton, 1973; Saffer and Marone, 2003; Yashima et al., 2015; Kurzawski et al., 2018). In addition, 7 datasets contain measurements at more than 60 different loads (Lilly, 1982; Schellart, 2000; Kurzawski et al., 2018). Numerous other studies constrain the temperature, slip-rate, pore-fluid pressure, and composition dependence of rock friction (e.g., He et al., 2006; Sone et al., 2012; den Hartog et al., 2012; Mitchell et al., 2013; Chen et al., 2015; Zhang et al., 2017; An et al., 2020;

Fagereng and Ikari, 2020; Okuda et al., 2021; Bedford et al., 2022; Ruggieri et al., 2024; DiMonte et al., 2025, and references therein) or the underlying physics (e.g., Lu et al., 2007; Nagata et al., 2008; Yamashita et al., 2014; Veedu and Barbot, 2016; Kilgore et al., 2017; Shreedharan et al., 2019; Mele Veedu et al., 2020; Gvirtzman and Fineberg, 2021), but do not provide systematic exploration of frictional strength as a function of effective normal stress.

The experimental findings are summarized in Figure 1 in a linear x-y plot, compatible with common practice. Although a linear model incorporating a cohesion term can approximate frictional behavior reasonably well within the 100–700 MPa range (Byerlee, 1978), this representation fails critically at lower stresses. Accordingly, the piecewise linear model proposed by Byerlee (1978) does not include cohesion at vanishing normal stress, consistent with the data available at the time (Barton, 1973, 1976; Handin, 1969; Hoskins et al., 1968; Jaeger, 1959; Murrell, 1965). Detailed analysis of the 0–50 MPa and 0–10 MPa regimes for all datasets demonstrates the absence of residual strength at vanishing normal stress, contradicting the cohesion hypothesis derived from high-pressure data. Furthermore, the friction coefficients may exceed 2 in low-stress experiments, providing unambiguous evidence for strong normal stress dependence of the friction coefficient. The dataset highlights a fundamental nonlinear relationship between strength and effective normal stress, as previously noted (Pascoe and Tabor, 1956; Archard, 1957; Jaeger, 1959; Murrell, 1965; Barton, 1976; Byerlee, 1978; Lilly, 1982; Jang and Jang, 2014; Barbot, 2024a).

Inspection of individual datasets in more detail provides further insights. Consider first the frictional resistance of Bilsthorpe silty mudstone fractures (Barton, 1973) over a range of normal stress from 0.8 MPa to 45 MPa (Figure 2). Although a linear model captures the overall increase of the frictional resistance with normal stress, some systematic misfits occur, particularly at low normal stress. Comparison of the linear and power-law models with an F-test, considering the two degrees of freedom of each model, leads to the rejection of the linear model with 87% confidence. Such results are typical of experimental data covering a wide range of normal stress (Figure 3). The friction coefficient of Hucknall shale (Barton, 1973) appears linear in log-log space, although more variability appears at low normal stress. Although the linear model constitutes an adequate approximation of frictional strength over a limited range of normal stress, it cannot simultaneously explain low-pressure and high-pressure data covering two orders of magnitude of normal stress. Comparison of the linear and power-law models for Hucknall shale with an F-test leads to the rejection of the linear model with 99% confidence. Application of the F-test on the linear and power-law models of the Ormonde silstone and Bilsthorpe mudstone leads to the rejection of the linear model with 89% and 99.7% confidence, respectively.

The friction coefficient of Darley Dale sandstone, containing some 75% quartz and 15% feldspars, shows a similar linear trend in log-log space, which is poorly captured by the linear model (Figure 3). For Darley Dale sandstone, the linear and power-law models lead to variance reductions of 88.8% and 99.9%, respectively, leading to a rejection of the linear model with 91.1% confidence based on an F-test. Byerlee (1978) explained the frictional resistance of Bilsthorpe mudstone and silty mudstone, Ormonde siltstone, Hucknall shale, and Darley Dale sandstone with a piecewise linear model involving different sensitivities to normal stress in different stress regimes featuring zero cohesion at low normal stress. However, the empirical model features discontinuous derivatives at the boundary of stress regimes, making it ill-suited for numerical applications, and implies a constant friction coefficient at low normal stress, in stark contrast with the continuous dependence on normal stress observed experimentally. The normal stress dependence of the frictional resistance of various polymers (Pascoe and Tabor, 1956), engineered surfaces (Archard, 1957), Beekmantown dolomite, Berea sandstone, and Seminole shale (Maurer, 1965), Darley Dale sandstone (Murrell, 1965), siltstone, mudstone, shale, and mudstone (Hobbs, 1966, 1970), and Mt McRae shale (Lilly, 1982), motivated these and other workers to consider a power-law model for the frictional resistance of fractured rocks, invoking a physical underpinning in the real area of contact.

I further illustrate the shortcomings of the linear model and the adequacy of the power-law model using experimental data on fine sand powder at normal stress below 1 kPa (Schellart, 2000) in Figure 4. In this range of normal stress, the frictional coefficient of sand powder varies from 1 to above 2. The frictional strength shows a downward curvature compatible with a decrease of the friction coefficient with increasing normal stress and the absence of significant cohesion. The linear model with cohesion produces systematic residuals at low normal stress. Comparison of the linear and power-law models with an F-test suggests the rejection of the linear model with 97.6% confidence. Other experiments indicate the absence of significant cohesion at low effective normal stress, including Inada granite, Orikabe monzonite, Manazuru andesite, Mizuho trachyte, tuff, slate, Solenhofen limestone, Dunham dolomite, serpentinite, and Yamaguchi calcite marble at 1–100 MPa (Ohnaka, 1975), quartz, microcline feldspar, chlorite, and phlogopite at 0.5–5 MPa (Horn and Deere, 1962), shale at 0.2–1.2 MPa (Lilly, 1982), and limestone at 0.5–3 MPa (Sanei et al., 2015).

These findings fundamentally challenge the conventional linear friction model with cohesion. A linear model fails to describe low-stress behavior where cohesion is demonstrably absent and it cannot simultaneously account for the high friction coefficients observed at low stresses. Although piecewise linear approximations offer some improvement (Byerlee, 1978), they introduce unnecessary complexity through multiple empirical parameters without providing much insights into the underlying physical mechanisms. However, the failure of the linear model is more profound when considering water-saturated phyllosilicate-rich fractures.

The power-law dependence of rock friction on effec-

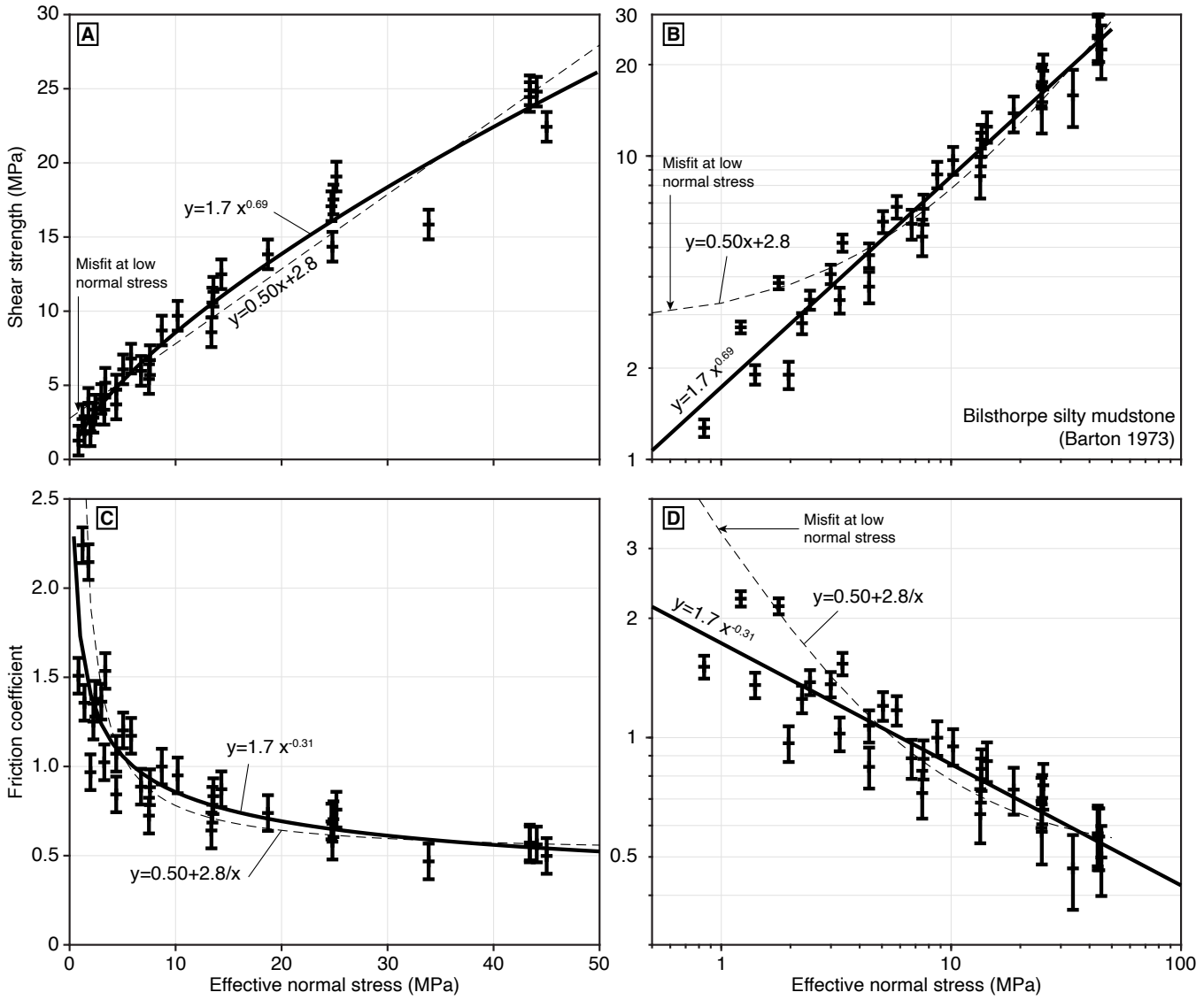

Figure 2 Comparison of linear and power-law models for rock friction. The frictional strength of Bilsthorpe silty mudstone (Barton, 1973) can be explained with a linear dependence with normal stress (dashed lines) or with a power-law dependence of normal stress (solid line), leading to a variance reduction of 98% and 98.9%, respectively. A, B) Frictional strength in linear and log-log plots, respectively. C, D) Friction coefficient in linear and log-log plots, respectively. The linear model gives rise to systematic residuals at low normal stress. Based on an F-test, one can reject the linear model with 87% confidence for these data.

tive normal stress is particularly well illustrated for dry and water-saturated montmorillonite (Morrow et al., 2017) as experimental conditions cover two orders of magnitude of effective normal stress (Figure 5). In dry conditions, montmorillonite is strong with a friction coefficient decaying with increasing normal stress. In contrast, the frictional strength of water-saturated montmorillonite is weak and features a parabolic profile with effective normal stress. The application of the linear model suggests a negative frictional strength for sufficiently low effective normal stress, associated with a negative intercept at the origin. As the intercept of the linear model is often interpreted as the cohesion of the interface, the prediction of the linear model is unphysical. Even though the linear model captures the overall frictional strength of water-saturated montmorillonite well, with a variance reduction of 99%, the power-law model performs even better, showcasing a variance reduction of 99.6%. Comparison of the linear and power-law models for water-saturated montmorillonite with an F-test allows us to discard the linear model with 94% confidence.

The shortcomings of the linear model for montmorillonite friction are representative of phyllosilicate-rich gouge, which is often found in fault zones due to deformation-assisted water alteration. Phyllosilicate-rich gouge often features a parabolic strength profile associated with the increase of the friction coefficient with effective normal stress. I illustrate this effect for argillite, tremolite schist, cataclasite, and talc schist (Hirauchi et al., 2020b) in Figure S5. In all cases, the linear model predicts negative strength at sufficiently low effective normal stress and suggests a negative cohesion, two unphysical features. As a result, the linear model is generally inadequate to explain the frictional properties of phyllosilicate-rich gouge, except for a limited range of effective normal stress as an approximation. The power-law model, in contrast, perfectly explains

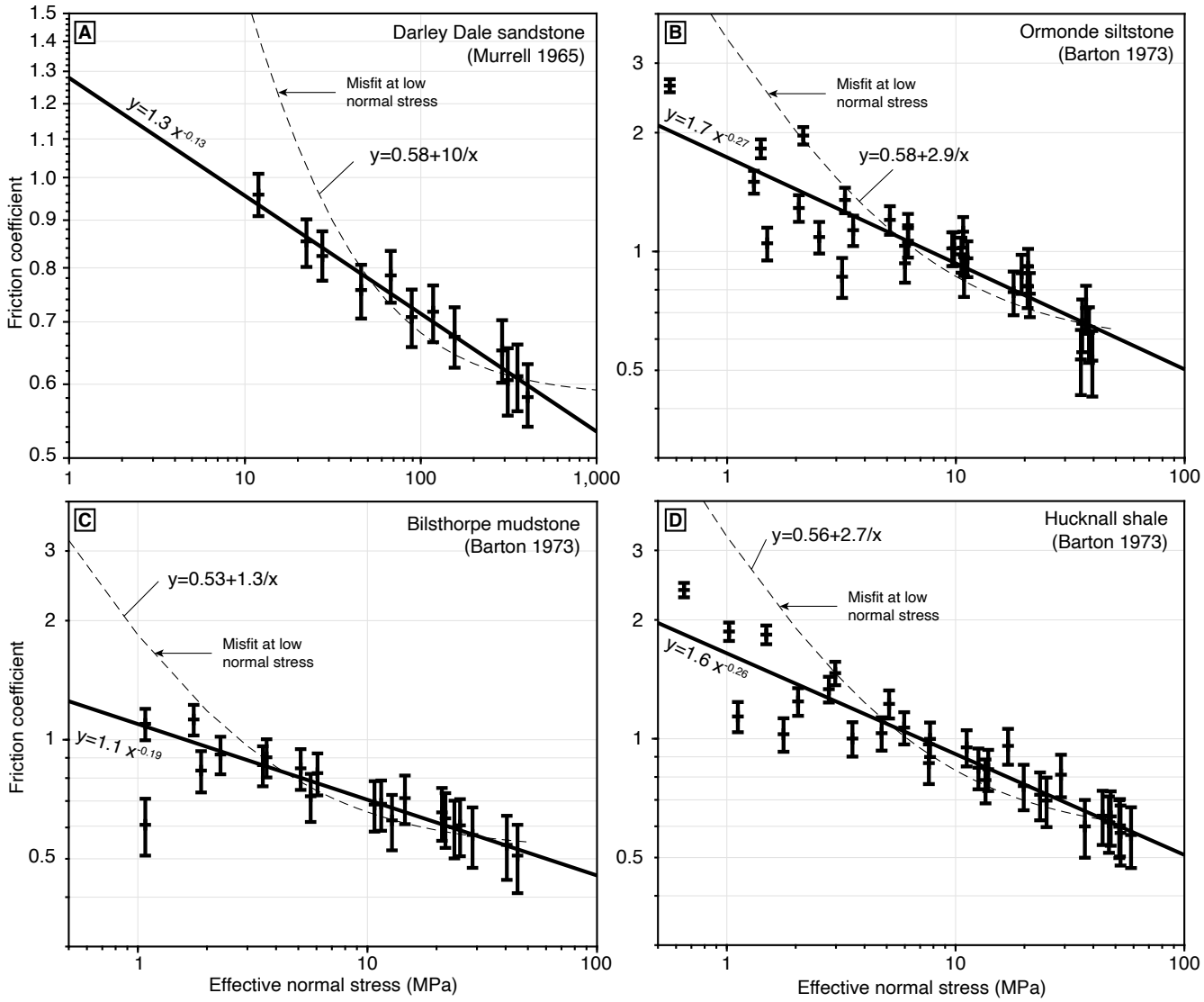

Figure 3 Comparison of linear and power-law models for the frictional resistance of Darley Dale sandstone (Murrell, 1965), and Ormonde siltstone, Bilsthorpe mudstone, and Hucknall shale (Barton, 1973). A) For Darley Dale sandstone, the linear and power-law models lead to variance reductions of 88.8% and 99.9%, respectively. The linear model can be rejected with 91.1% confidence. B) For the frictional strength of Ormonde siltstone (Barton, 1973), the linear and power-law models give rise to a variance reduction of 97.5% and 98.4%, respectively. Using an F-test, one can reject the linear model with 89% confidence. The increase in data variance at low normal stress may be caused by the lower accuracy of triaxial apparatuses at diminishing pressure. C) For Bilsthorpe mudstone (Barton, 1973), the linear and power-law models give rise to a variance reduction of 99.4% and 99.8%, respectively and one can reject the linear model with 99.7% confidence based on an F-test. D) The frictional strength of Hucknall shale (Barton, 1973) can be explained with a linear dependence with normal stress (dashed lines) or with a power-law dependence of normal stress (solid line), leading to a variance reduction of 99.2% and 99.7%, respectively. Based on an F-test, one can reject the linear model with 99% confidence. In all cases, the linear model gives rise to systematic residuals at low normal stress. The best-fitting parameters are indicated in the equations. Further illustrations of the data are shown in Figures S1–S4.

the mechanical data (100% variance reduction) and predicts positive strength at all effective normal stress.

Collectively, these results indicate the inadequacy of the linear model for experimental conditions covering a wide range of normal loads, and for rocks that feature increasing friction coefficient with effective normal stress, such as phyllosilicates or phyllosilicate-rich rocks in water-saturated, low-temperature conditions. In contrast, the power-law model performs well for dry and water-saturated phyllosilicate, and for other rocks or gouge across a wide range of normal loads. Next, I test whether the power-law model is compatible with experimental constraints for a wider range of lithologies.

3 Characteristics of power-law friction

Figure 6 presents the experimental dataset in Table 1 in log-log coordinates, revealing consistent power-law scaling of frictional strength with effective normal stress across all 119 experiments. The consistent behavior for effective normal stresses ranging from 10 Pa to 1 GPa indicates the continuity of the underlying mechanical process. Although strength generally increases with normal stress, the relationships display

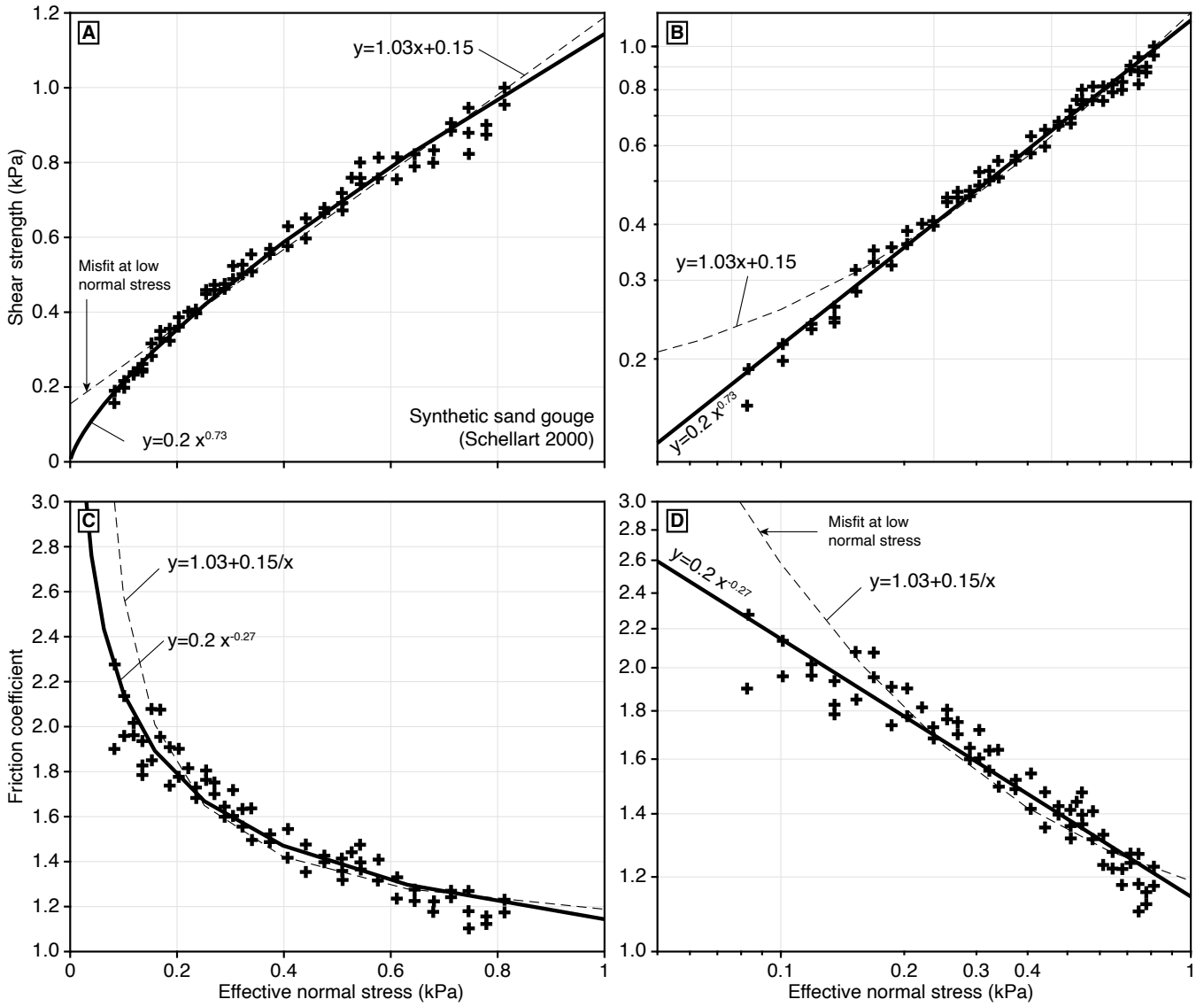

Figure 4 Comparison of linear and power-law models for synthetic sand gouge (Schellart, 2000) at low effective normal stress. The frictional strength of synthetic sand powder (black triangles) can be explained with a linear dependence with normal stress (dashed lines) or with a power-law dependence of normal stress (solid line), leading to a variance reduction of 99.6% and 99.8%, respectively. The best-fitting parameters are indicated in the equations. A, B) Frictional strength in linear and log-log plots, respectively. C, D) Friction coefficient in linear and log-log plots, respectively. The linear model gives rise to systematic residuals at low normal stress. Based on an F-test, one can reject the linear model with 97.6% confidence.

systematic deviations from linearity, manifesting sub-linear and superlinear behaviors. Following Pascoe and Tabor (1956), Archard (1957), Murrell (1965), Maurer (1965), Hobbs (1966, 1970), Lilly (1982), and Barbot (2024a), I consider a unified power-law description of the friction coefficient over the full range of effective normal stress as follows

$$\mu = \mu_0 \left(\frac{\bar{\sigma}}{\sigma_0} \right)^{-\beta} , \qquad (1)$$

where μ_0 represents the friction coefficient at the normalization stress $\sigma_0 = 1$ MPa, $\bar{\sigma}$ is the effective normal stress incorporating pore-fluid pressure effects, and β is a power-law exponent that quantifies the normal stress dependence. The model captures frictional strength across the entire range of effective normal stress with only two degrees of freedom. The scaling factor σ_0 is merely a reference value defining μ_0 and the relevant physical unit for the effective normal stress, as power laws should only take non-dimensional arguments, that is, $\mu = \mu_0$ at $\bar{\sigma} = \sigma_0$. Any other real positive reference value σ_1 is acceptable, as in $\mu = \mu_1(\bar{\sigma}/\sigma_1)^{-\beta}$, without affecting the model prediction. In that case, the new reference friction coefficient can be calculated directly as $\mu_1 = \mu_0(\sigma_0/\sigma_1)^{\beta}$.

I now systematically analyze the dataset to determine the non-dimensional parameters μ_0 and β for each material, examining potential correlations with lithology and physical properties. I inspect the characteristics of power-law friction for rocks, synthetic gouge, and engineered surfaces. For each dataset, I estimate the constitutive parameters in Equation (1) using the best linear unbiased estimator. Bootstrap analyses by leaving out 5 to 10 samples indicate uncertainties of the order of 0.05 and 0.02 for μ_0 and β, respectively. The uncertainty on β is reduced to ± 0.01 when only one sample is ran-

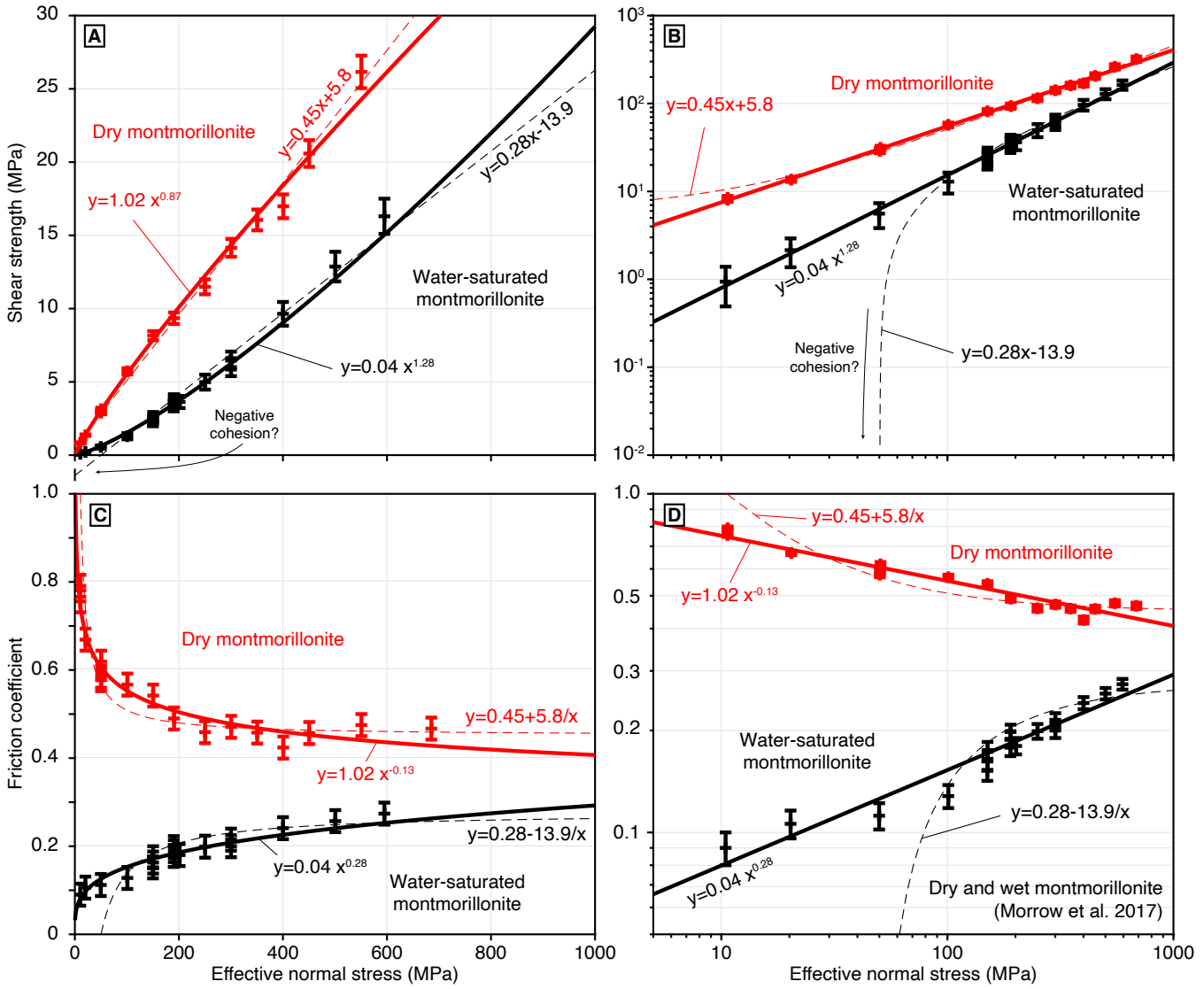

Figure 5 Comparison of linear and power-law models for dry and water-saturated montmorillonite (Morrow et al., 2017). A) Frictional strength of oven-dry (red) and water-saturated (black) montmorillonite and corresponding linear (dashed lines) and power-law (solid lines) models. For water-saturated montmorillonite, the best-fitting linear model predicts negative strength close to the origin, associated with a negative intercept. B) Frictional strength for dry and water-saturated montmorillonite in log-log plots, emphasizing the systematic residuals at low normal stress. C, D) Friction coefficient in linear and log-log plots, respectively. The power-law model explains dry and water-saturated montmorillonite satisfactorily, and does not feature systematic residuals.

domly taken out. Expectedly, datasets with fewer measurements produce more uncertainties during parameter estimation. The best-fitting parameters are listed in Table S1 showing three significant digits of accuracy. For clarity, I show the samples with a diminishing function of effective normal stress in Figure 7 and those with an increasing function of effective normal stress in Figure 8.

On average, the samples in Figure 7 feature power-law exponents $\beta = 0.21 \pm 0.12$. The normal stress dependency is well resolved for each sample. Westerly granite features the power-law exponent $\beta = 0.133 \pm 0.003$. The strength of ice at 77 K is associated with the exponent $\beta = 0.31 \pm 0.002$. Natural fault gouge from the Caleta Coloso Fault (CFF) features the exponents $\beta = 0.30 \pm 0.008$ and $\beta = 0.25 \pm 0.008$. The green cataclasites from the Moonlight fault zone showcase $\beta = 0.19 \pm 0.005$. Ice friction features extreme sensitivity to normal stress, with $\beta = 0.59$ and $\beta = 0.41$ for intermediate and fast sliding. Among silicate rocks, the power-law dependence is most dramatic for Solenhofen sandstone, best characterized by $\beta = 0.43 \pm 0.01$. Such acute sensitivity to normal stress gives rise to friction coefficient above 1 at low stresses for Solenhofen sandstone, Ormonde siltstone, Bilsthorpe silty mudstone, Hucknall shale, trachyte, and Wombeyan marble. Natural samples from the Paposo Fault (PPF10) and Weber sandstone C feature the most linear behavior, with $\beta = 0.02$ and $\beta = 0.04$, respectively. Clearly, a power-law relationship encompasses the linear case without cohesion for $\beta = 0$.

The samples in Figure 8 sometimes feature a dramatic increase of the friction coefficient with increasing effective normal stress. For example, the friction coefficient of chrysotile at 100°C increases three-fold from 40 to 200 MPa. The effect diminishes with increasing temperature (Moore et al., 2004). The friction coefficient of terrigenous silty clay 2H1 (Kurzawski et al., 2018) jumps

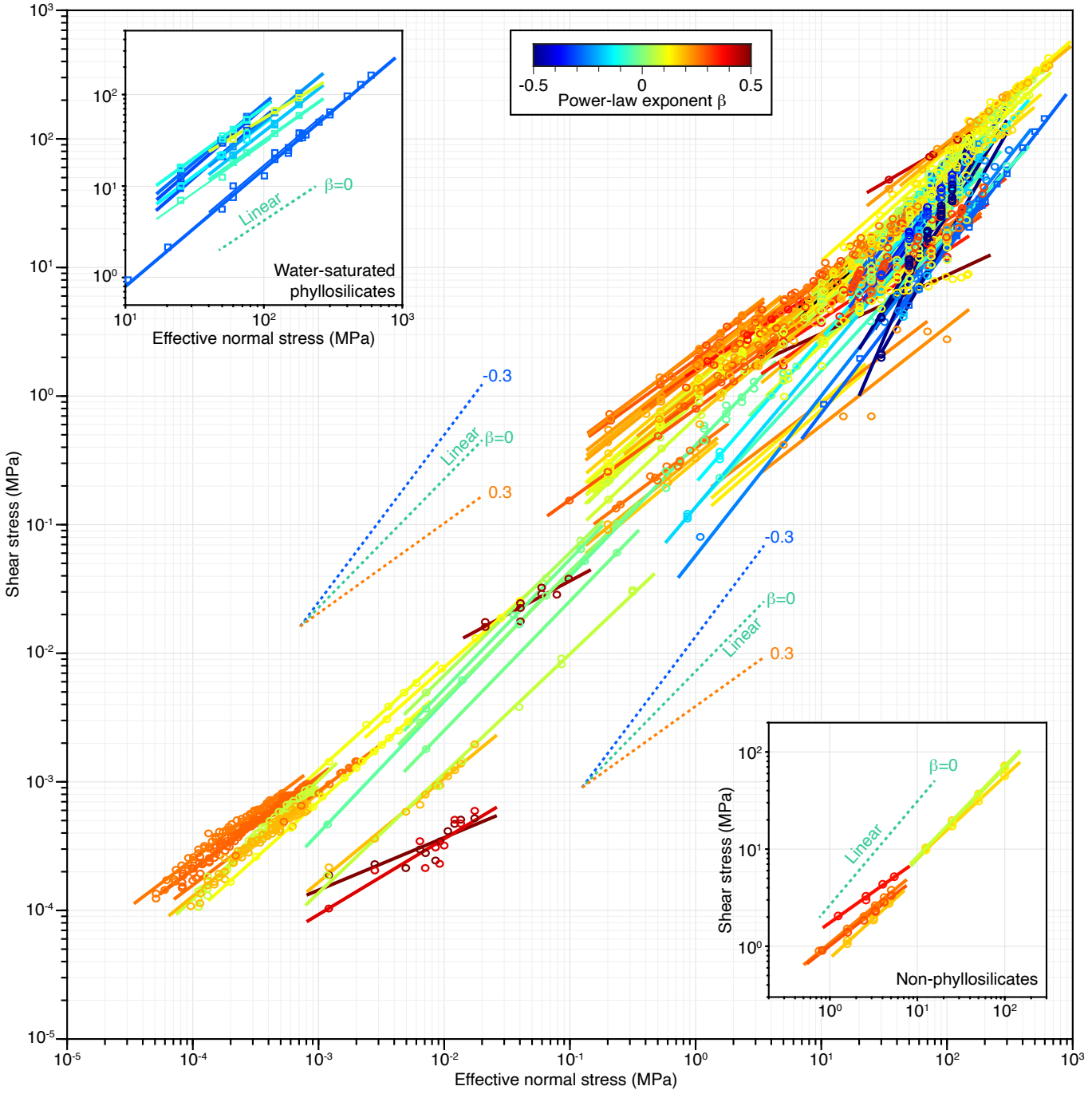

Figure 6 Sliding friction of rocks from the experimental studies listed in Table 1, plotted in log-log coordinates. The colored lines correspond to the least-squares best-fitting power-law model of Equation (1), colored by the power-law exponent β. The dashed lines indicate sublinear, linear, and superlinear relationship for power-law exponents of 0.7, 1.0, and 1.3. All the data are well explained by a power-law relationship.

from 0.08 at 30 MPa to 0.5 at 110 MPa, corresponding to a power-law exponent $\beta = -1.28$, the most negative value documented to date. The increase of the friction coefficient is observed in natural and synthetic gouge. For example, pure montmorillonite in water-saturated conditions (Morrow et al., 2017) showcases $\beta = -0.28$. Synthetic mixtures of 20% talc and 80% calcite feature $\beta = -0.04$. The power-law relationship holds for a wide range of mineral composition.

The samples with increasing friction coefficient have overall low strength and consist mostly of pure phyllosilicate gouge, including pure montmorillonite, muscovite, talc, biotite/phlogopite, chrysotile serpentine in water-saturated conditions, phyllosilicate-rich natural gouge, such as the chlorite and talc phyllonite from the Zuccale fault (Smith and Faulkner, 2010), or mixtures of minerals with a high concentration of phyllosilicates (Giorgetti et al., 2015). Some samples, such as the amphibole schist, foliated cataclasite, and chlorite-rich dry fault gouge (Smith and Faulkner, 2010), stand out for featuring an overall high coefficient of friction that increases with effective normal stress. The peculiar frictional behavior of phyllosilicates with an overall low strength and a coefficient of friction that increases with effective normal stress is thought to originate from osmotic pressure around contact junctions, which re-

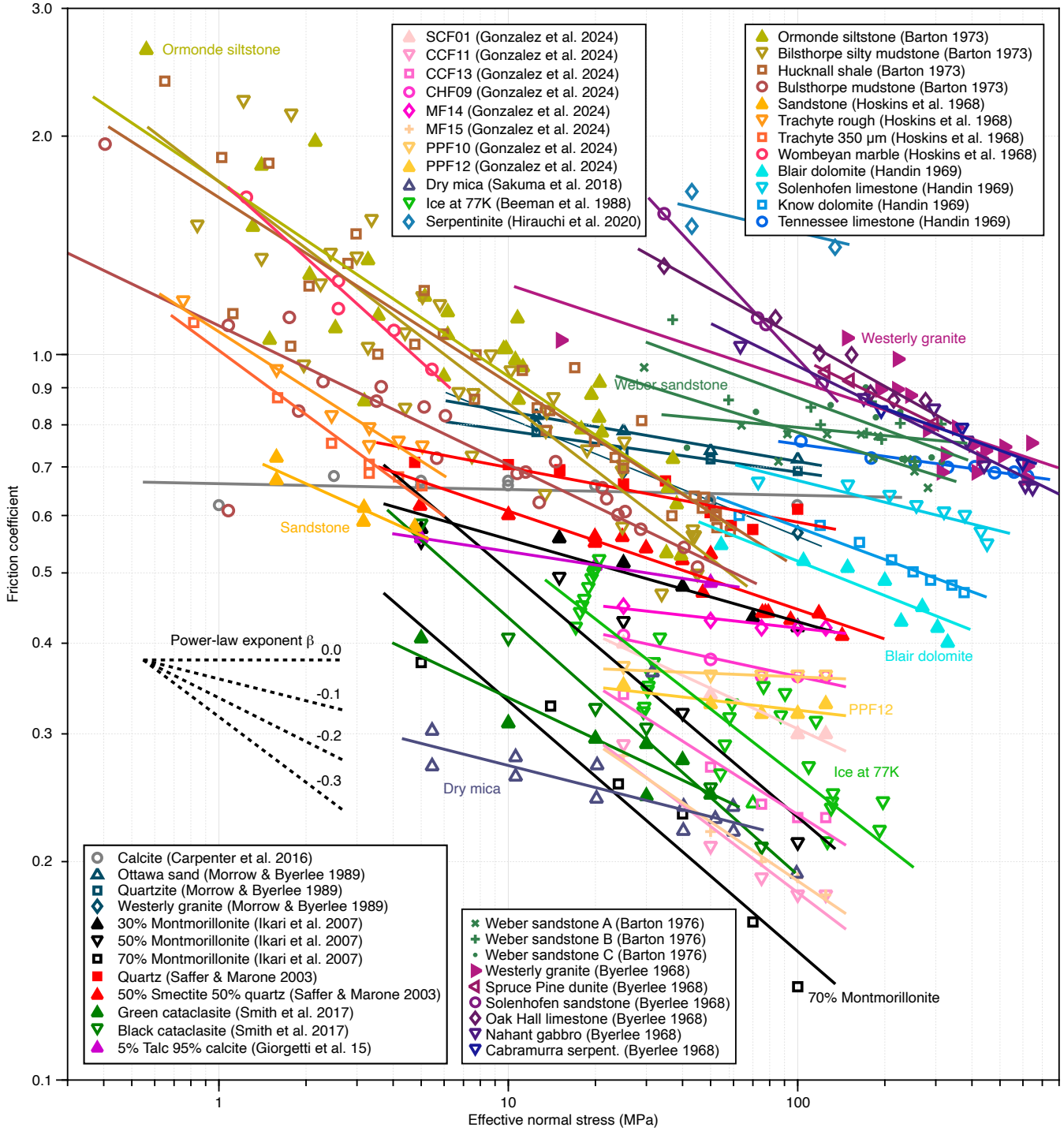

Figure 7 Friction coefficient for natural and synthetic gouge decreasing with effective normal stress, mostly framework silicates. The solid lines correspond to the best-fitting power-law relationship of Equation (1). The power-law exponents for the effective normal stress dependency fall within $\beta = 0.21 \pm 0.12$ on average for all samples.

duces the real area of contact (Renard and Ortoleva, 1997; Moore and Lockner, 2007; Beynon and Faulkner, 2020). Hence, while water-saturated phyllosilicates are weak and feature increasing friction coefficient with effective normal stress, dry phyllosilicates are strong and feature decreasing friction coefficient with effective normal stress (Morrow et al., 2017; Beynon and Faulkner, 2020). Phyllosilicate-rich gouge inherit this property, granted a sufficiently high concentration of clay minerals.

Although not immediately relevant to earthquake science, experiments on synthetic materials provide important physical insights. Same as natural and synthetic gouge, the friction coefficient of most synthetic materials considered in the study feature a strong dependency with normal stress (Figure S7). The experiments on caster sugar and sand (Schellart, 2000), polydimethylsiloxane (PDMS) and glass spheres (Maegawa et al., 2015; Yashima et al., 2015) mostly feature $\beta > 0.1$, compatible with rock friction. The experiments on pine wood, elm wood, oak wood and a bimaterial interface made of oak and pine wood by Coulomb (1821) feature

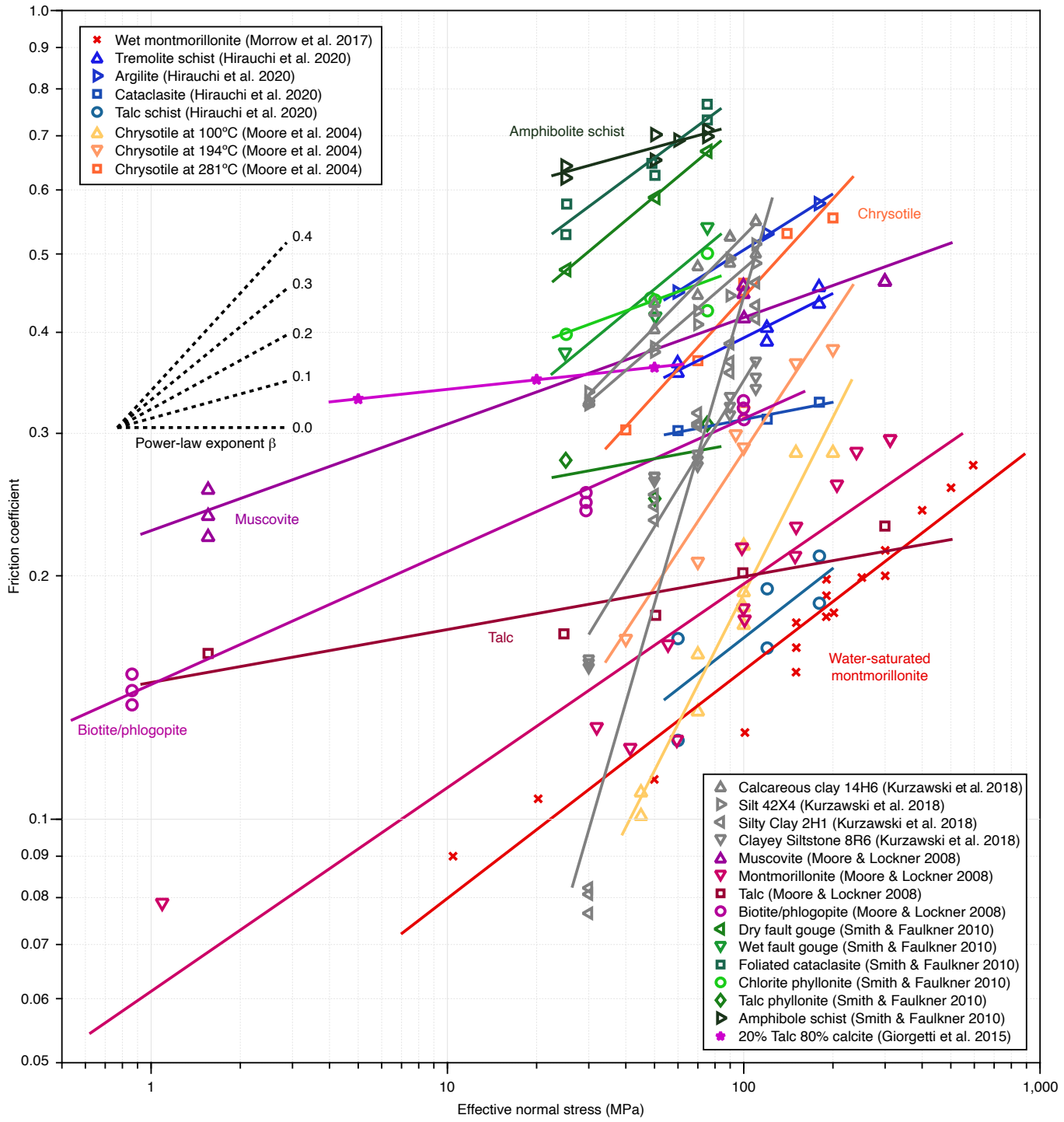

Figure 8 Friction coefficient for natural and synthetic gouge increasing with effective normal stress, mostly phyllosilicate-rich gouge. The solid lines indicate the best-fitting power-law relationship following Equation (1). The power-law exponents for the effective normal stress dependency fall within $\beta = -0.224 \pm 0.18$ on average for all samples, highlighting a high variability.

a low stress dependency of the friction coefficient (Table S1). The large variability of oak wood friction is associated with measurements conducted after hours of stationary rest, resulting in healing of the interface and elevated strength, and others conducted during high-speed, low-strength sliding. Despite the difference in materials, the power-law model explains these experimental data consistently from 10 Pa to 1 MPa.

4 Discussion

A linear model for sliding friction is only accurate for a limited range of normal loads and makes physically invalid predictions for an important class of rocks incorporating phyllosilicates in water-saturated conditions. Although cohesion makes an important contribution in the strength of intact rocks before failure, it seems to play a negligible role in the sliding friction of pre-existing fractures based on available experimental data. The adequacy of power-law friction to explain natu-

ral and synthetic gouge, ice, and engineered surfaces points to a universal underlying process. Direct observations from experiments on transparent materials provide a robust explanation for power-law friction. Although the friction coefficient scales linearly with the real area of contact (Maegawa et al., 2015), the real area of contact itself follows a power-law dependence on effective normal stress (Figure 9). The real area of contact of polymethyl methacrylate (PMMA), calcite, glass, and quartz surfaces (Dieterich and Kilgore, 1994) follows a power-law with exponents 0.85, 0.69, 0.69, and 0.73, respectively, of the same order as the power-law exponent of fractured rocks in Table S1. Similarly, experiments on PMMA spherical rods under normal load show the real area of contact following a power-law with exponent 0.72 (Archard, 1957). The real area of contact of engineered surfaces made of polydimethylsiloxane (PDMS) asperities in contact with glass spheres or glass asperities in contact with PDMS (Yashima et al., 2015) follows a power-law dependence on normal stress over two orders of magnitude, with power-exponents ranging from 0.82 to 0.94. The power-law dependence of the real area of contact on normal stress is expected for a Hertzian (spherical, elastic) contact (Hertz, 1881), even in the presence of roughness (Archard, 1957).

As noted previously (Pascoe and Tabor, 1956; Archard, 1957; Jaeger, 1959; Murrell, 1965; Barton, 1976; Byerlee, 1978; Lilly, 1982; Jang and Jang, 2014; Barbot, 2024a), the physical underpinning of the power-law dependence is a linear dependence of the frictional resistance with the real area of contact and the power-law dependence of the real area of contact with effective normal stress. The different mechanical behavior of water-saturated phyllosilicates, with a friction coefficient that increases with effective normal stress, originates from osmotic pressurization of the mineral surface near contact junctions that increases with confining pressure (Renard and Ortoleva, 1997; Moore and Lockner, 2007; Beynon and Faulkner, 2020). Physical models of rock friction based on the real area of contact calibrated with these observations capture the direct, evolutionary, and steady-state strength of rocks upon perturbations of effective normal stress (Barbot, 2024a, 2025). Incorporating the relationship into constitutive model of rock friction explains the origin of the state dependence of friction (Barbot, 2019; Wu and Barbot, 2025) and reproduces deformation data across broad conditions of slip-rate, temperature, and effective normal stress (Barbot, 2019, 2024b; Guvercin et al., 2025). Such physical models of rock friction capture stability transitions as a function of temperature and slip-rate (Barbot, 2022, 2023; Nie and Barbot, 2024), the brittle-ductile transition (Barbot, 2023; Barbot and Zhang, 2023), and the evolution of the real area of contact during quasi-static and dynamic ruptures (Wu and Barbot, 2025). Hence, the nonlinear nature of the frictional resistance is well understood conceptually. The normal stress dependence of the steady-state friction coefficient, directly controlled by the real area of contact, and by osmotic pressure for phyllosilicates, is also indirectly affected by the pressure-dependent healing process (Barbot, 2024a) and by the pressure dependence of the thermal activation (Barbot et al., 2025). The multiple factors involved in the normal-stress dependence of the friction coefficient help explain the variability of the experimental observations.

The strong agreement between experimental observations and theory provides a robust conceptual understanding of the nonlinear nature of frictional resistance, establishing power-law friction as a fundamental description of shear failure on pre-existing fractures across scales and materials. Analyzing rock friction data in linear coordinates can be misleading, as it artificially suggests distinct mechanical processes for different normal stress regimes to account for the varying friction coefficients. Although different healing mechanisms may indeed operate at different pressure conditions (Barbot et al., 2025), the continuous normal stress dependence of the friction coefficient is the norm, not the exception. Additionally, a linear interpretation of high-pressure data incorrectly suggests a contribution of cohesion, which is clearly negligible in low-pressure data. In contrast, log-log representations reveal the stationarity of the frictional behavior across all stress conditions without significant cohesion, simplifying the physical interpretation.

As earthquakes and slow-slip events may operate under low effective normal stress due to over-pressurized pore fluids, capturing the evolution of frictional stress at low pressure is paramount. The limited contribution of cohesion in laboratory experiments across different scales and materials suggests a limited role of cohesion healing during the seismic cycle (Jeppson et al., 2023). However, cohesion may still play an important role in natural faults, especially under the high-temperature, high-pressure conditions of the middle crust where cementation and lithification may be efficient at the time scales of the interseismic period of the seismic cycle, as suggested by Thomas et al. (2025). Experiments on wet Pozzolanic mortar involving holds longer than 3,000 s in quasi-stationary contact indicate a contribution of cohesion of the order of tens of kPa (Volpe et al., 2026) (Figure S6). Although this is not apparently the case for any of the experiments shown in this study, the normal-stress dependence of rock friction may evolve in various conditions of pressure, leading to distinctly different trends in log-log space in various stress conditions. This behavior may be caused by experimental bias, for example the residual jacket strength at low normal stress discussed by Behnsen and Faulkner (2012). Additional effects include change of dominant healing mechanism, with rates following different normal stress dependencies (Barbot et al., 2025). In this case, the change of normal stress dependence can be associated with a stability transition, as for smectite clay (Saffer et al., 2001). These differences, albeit rare, do not imply a shortcoming of power-law friction but require a more detailed model capturing temperature and pressure effects.

5 Conclusions

A comprehensive analysis of experimental rock friction data reveals a power-law relationship between frictional

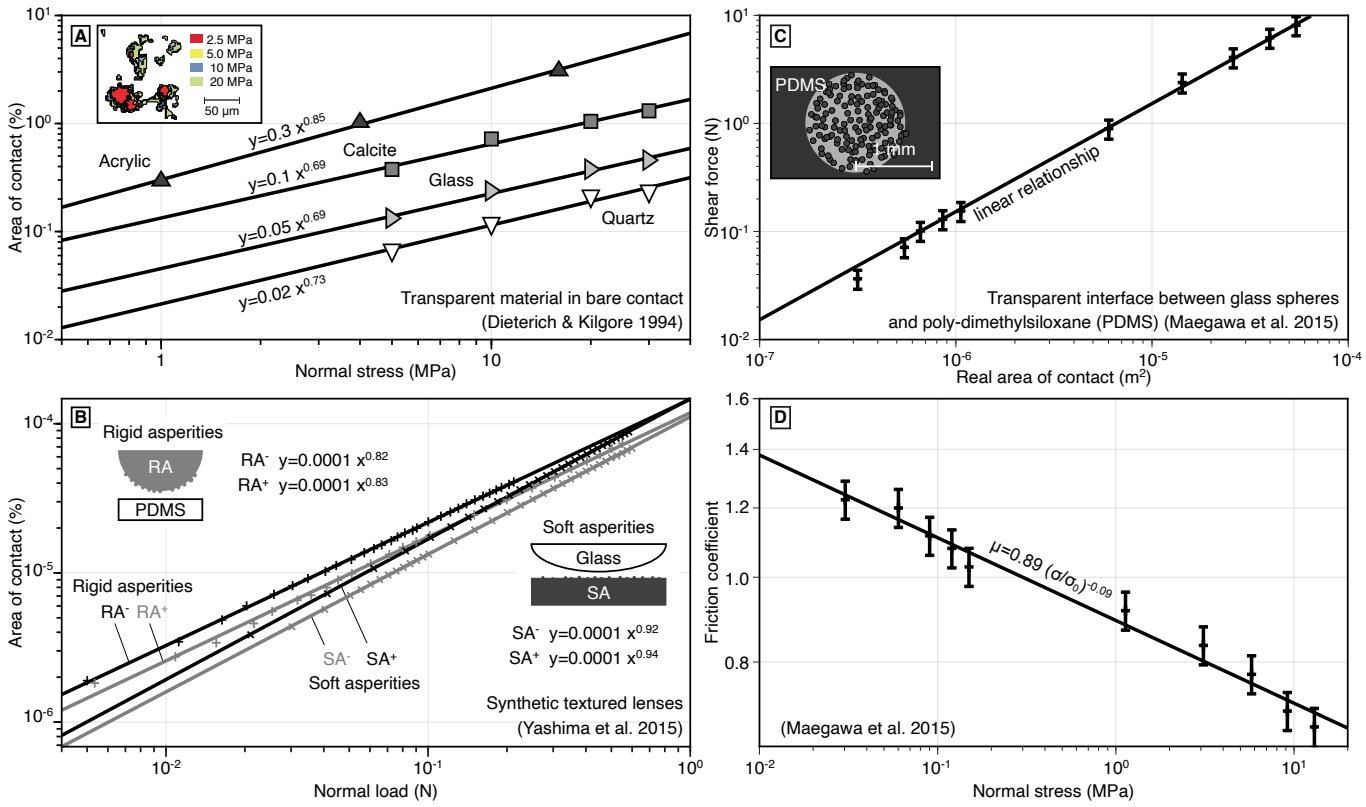

Figure 9 Normal stress dependence of the real area of contact and origin of power-law friction. A) Evolution of the real area of contact in rough acrylic, calcite, glass, and quartz surfaces as a function of normal stress (Dieterich and Kilgore, 1994), associated with power-law exponents 0.85, 0.69, 0.69, and 0.73, respectively. The inset shows the morphology of micro-asperities forming the contact junctions at various normal loads. B) Real area of contact for engineered rigid asperities (RA) made of glass with micro-lenses in contact with nominally flat polydimethylsiloxane (PDMS), and for soft (low-rigidity) asperities (SA) in PDMS in contact with a nominally flat spherical glass lense as a function of normal load (Yashima et al., 2015). The subscripts + and - are for large and small micro-lenses, respectively. The real area of contact follows power-law exponents of 0.82, 0.83, 0.92, and 0.94 for RA^-, RA^+, SA^-, and SA^+, respectively. C) Frictional resistance dependence on the real area of contact for transparent interface between glass spheres and poly-dimethylsiloxane (PDMS) (Maegawa et al., 2015), featuring a linear relationship over two orders of magnitude. D) Coefficient of friction of the same interface as a function of normal stress, indicating that the real area of contact of the PDMS interface is a power-law of normal stress.

strength and effective normal stress across broadly different materials, including silicates, ice, natural and synthetic gouge, and engineered surfaces, spanning a stress range over seven orders of magnitude, irrespective of testing apparatus.

The power-law friction exponent β is positive for most non-phyllosilicate rocks and engineered surfaces, but is negative for water-saturated phyllosilicates. The power-law scaling arises from the real area of contact and its nonlinear dependence on normal stress. At steady-state, the normal stress dependence of friction is further affected by the pressure dependence of healing. The weakness and characteristic stress dependence of phyllosilicates is presumably due to osmotic pressure near contact junctions, highlighting the controls of mineralogy and fluid content.

The study underscores the inadequacy of linear friction laws and advocates for the adoption of power-law constitutive models in earthquake mechanics. Cohesion, often invoked in linear models, is negligible at macroscopic scales. Power-law friction reconciles disparate observations, eliminating the need for ad hoc piecewise linear models, and provides a unified basis for modeling fault mechanics across tectonic settings.

Constitutive laws that ignore the normal-stress dependency of the friction coefficient fundamentally misrepresent the underlying phenomenology, with implications for earthquake mechanics. Local linear approximations may be acceptable in some circumstances, particularly at high effective normal stress, but the parameters involved do not directly reflect the physical properties of rocks, as they vary with the point of expansion or the range of applicability. The friction coefficient is a continuous function of effective normal stress. As constitutive models of rock friction capture the phenomenology with increasing accuracy, future work should explore the impact of the lithology and physical condition of fault zones on rupture style and seismic hazards.

Acknowledgments

I am grateful for the experimental work of many scientists across decades who have produced high-quality data, without which this work would not be possible. I acknowledge the constructive comments from Editor Prof. Åke Fagereng and two anonymous reviewers.

Competing interests

There are no competing interests.

Data availability

A repository containing all the data in digital form and the visualization scripts used in this study are available in a zenodo repository (Barbot, 2026).

References

An, M., Zhang, F., Elsworth, D., Xu, Z., Chen, Z., and Zhang, L. Friction of Longmaxi Shale Gouges and Implications for Seismicity During Hydraulic Fracturing. *Journal of Geophysical Research: Solid Earth*, 125(8), Aug. 2020. doi: 10.1029/2020jb019885.

Archard, J. F. Elastic deformation and the laws of friction. *Proceedings of the Royal Society of London. Series A. Mathematical and Physical Sciences*, 243(1233):190–205, Dec. 1957. doi: 10.1098/rspa.1957.0214.

Barbot, S. Modulation of fault strength during the seismic cycle by grain-size evolution around contact junctions. *Tectonophysics*, 765:129–145, Aug. 2019. doi: 10.1016/j.tecto.2019.05.004.

Barbot, S. A Rate-, State-, and Temperature-Dependent Friction Law With Competing Healing Mechanisms. *Journal of Geophysical Research: Solid Earth*, 127(11), Nov. 2022. doi: 10.1029/2022jb025106.

Barbot, S. Constitutive Behavior of Rocks During the Seismic Cycle. *AGU Advances*, 4(5), Sept. 2023. doi: 10.1029/2023av000972.

Barbot, S. Transient and Steady-State Friction in Non-Isobaric Conditions. *Geochemistry, Geophysics, Geosystems*, 25(2), Feb. 2024a. doi: 10.1029/2023gc011279.

Barbot, S. Does the direct effect of friction increase continuously with absolute temperature? *Proceedings of the National Academy of Sciences*, 121(42), Oct. 2024b. doi: 10.1073/pnas.2405111121.

Barbot, S. The slip-rate, state-, temperature-, and normal-stress-dependence of fault friction. *Earthquake Science*, 38(4): 304–338, Aug. 2025. doi: 10.1016/j.eqs.2025.03.005.

Barbot, S. [Dataset] The normal stress dependence of rock friction, Feb. 2026. doi: 10.5281/zenodo.18393526.

Barbot, S. and Zhang, L. Constitutive Behavior of Olivine Gouge Across the Brittle-Ductile Transition. *Geophysical Research Letters*, 50(24), Dec. 2023. doi: 10.1029/2023gl105916.

Barbot, S., Guvercin, S. E., Zhang, L., Zhang, H., and Yang, Z. Thermobaric Activation of Fault Friction. *Geophysical Research Letters*, 52(6), Mar. 2025. doi: 10.1029/2024gl112959.

Barton, N. Review of a new shear-strength criterion for rock joints. *Engineering Geology*, 7(4):287–332, Jan. 1973. doi: 10.1016/0013-7952(73)90013-6.

Barton, N. The shear strength of rock and rock joints. *International Journal of Rock Mechanics and Mining Sciences & Geomechanics Abstracts*, 13(9):255–279, Sept. 1976. doi: 10.1016/0148-9062(76)90003-6.

Bedford, J. D., Faulkner, D. R., Allen, M. J., and Hirose, T. The stabilizing effect of high pore-fluid pressure along subduction megathrust faults: Evidence from friction experiments on accretionary sediments from the Nankai Trough. *Earth and Planetary Science Letters*, 574:117161, Nov. 2021. doi: 10.1016/j.epsl.2021.117161.

Bedford, J. D., Faulkner, D. R., and Lapusta, N. Fault rock heterogeneity can produce fault weakness and reduce fault stability. *Nature Communications*, 13(1), Jan. 2022. doi: 10.1038/s41467-022-27998-2.

Beeler, N. M., Tullis, T. E., and Goldsby, D. L. Constitutive relationships and physical basis of fault strength due to flash heating. *Journal of Geophysical Research: Solid Earth*, 113(B1), Jan. 2008. doi: 10.1029/2007jb004988.

Beeman, M., Durham, W. B., and Kirby, S. H. Friction of ice. *Journal of Geophysical Research: Solid Earth*, 93(B7):7625–7633, July 1988. doi: 10.1029/jb093ib07p07625.

Behnsen, J. and Faulkner, D. R. The effect of mineralogy and effective normal stress on frictional strength of sheet silicates. *Journal of Structural Geology*, 42:49–61, Sept. 2012. doi: 10.1016/j.jsg.2012.06.015.

Beynon, S. J. and Faulkner, D. R. Dry, damp, or drenched? The effect of water saturation on the frictional properties of clay fault gouges. *Journal of Structural Geology*, 140:104094, Nov. 2020. doi: 10.1016/j.jsg.2020.104094.

Bigaroni, N., Scuderi, M. M., Cappa, F., Guglielmi, Y., Nussbaum, C., Aldega, L., Pozzi, G., and Collettini, C. Frictional properties of Opalinus Clay: influence of humidity, normal stress and grain size on frictional stability. *Geophysical Journal International*, 233(1):211–228, Nov. 2022. doi: 10.1093/gji/ggac457.

Byerlee, J. *Friction of Rocks*, page 615–626. Birkhäuser Basel, 1978. doi: 10.1007/978-3-0348-7182-2_4.

Byerlee, J. D. Brittle-ductile transition in rocks. *Journal of Geophysical Research*, 73(14):4741–4750, July 1968. doi: 10.1029/jb073i014p04741.

Carpenter, B., Collettini, C., Viti, C., and Cavallo, A. The influence of normal stress and sliding velocity on the frictional behaviour of calcite at room temperature: insights from laboratory experiments and microstructural observations. *Geophysical Journal International*, 205(1):548–561, Feb. 2016. doi: 10.1093/gji/ggw038.

Carpenter, B. M., Marone, C., and Saffer, D. M. Frictional behavior of materials in the 3D SAFOD volume. *Geophysical Research Letters*, 36(5), Mar. 2009. doi: 10.1029/2008gl036660.

Chang, C., Noda, H., Hamada, Y., Huang, C., Ma, T., Wang, G., and Yamaguchi, T. Comminution-Induced Transient Frictional Behavior in Sheared Granular Halite. *Geophysical Research Letters*, 51(21), Nov. 2024. doi: 10.1029/2024gl109645.

Chen, J., Verberne, B. A., and Spiers, C. J. Effects of healing on the seismogenic potential of carbonate fault rocks: Experiments on samples from the Longmenshan Fault, Sichuan, China. *Journal of Geophysical Research: Solid Earth*, 120(8):5479–5506, Aug. 2015. doi: 10.1002/2015jb012051.

Coulomb, C. A. *Théorie des machines simples : en ayant égard au frottement de leurs parties et à la roideur des cordages*. Bachelier, 1821.

den Hartog, S. A., Peach, C. J., de Winter, D. M., Spiers, C. J., and Shimamoto, T. Frictional properties of megathrust fault gouges at low sliding velocities: New data on effects of normal stress and temperature. *Journal of Structural Geology*, 38:156–171, May 2012. doi: 10.1016/j.jsg.2011.12.001.

Di Toro, G., Hirose, T., Nielsen, S., Pennacchioni, G., and Shimamoto, T. Natural and Experimental Evidence of Melt Lubrication of Faults During Earthquakes. *Science*, 311(5761):647–649, Feb. 2006. doi: 10.1126/science.1121012.

Dieterich, J. H. and Kilgore, B. D. Direct observation of frictional contacts: New insights for state-dependent properties. *pure and applied geophysics*, 143(1–3):283–302, Mar. 1994. doi: 10.1007/bf00874332.

DiMonte, A. A., Ault, A. K., Shreedharan, S., and Hirth, G. Frictional Behavior of the Southern San Andreas Fault Reveals Ability to

Host Shallow Slow Slip Events. *Geophysical Research Letters*, 52 (12), June 2025. doi: 10.1029/2025gl116498.

Fagereng, Å. and Ikari, M. J. Low-Temperature Frictional Characteristics of Chlorite-Epidote-Amphibole Assemblages: Implications for Strength and Seismic Style of Retrograde Fault Zones. *Journal of Geophysical Research: Solid Earth*, 125(4), Apr. 2020. doi: 10.1029/2020jb019487.

Giorgetti, C., Carpenter, B. M., and Collettini, C. Frictional behavior of talc-calcite mixtures. *Journal of Geophysical Research: Solid Earth*, 120(9):6614–6633, Sept. 2015. doi: 10.1002/2015jb011970.

González, Y., González, G., Spagnuolo, E., Pozzi, G., Jensen, E., Aretusini, S., and Schleicher, A. M. Exploring frictional properties of upper plate fault reactivation in subduction zones: The Atacama Fault System in northern Chile. *Earth and Planetary Science Letters*, 648:119106, Dec. 2024. doi: 10.1016/j.epsl.2024.119106.

Guvercin, S., Barbot, S., Zhang, L., Yang, Z., Platt, J., Seyler, C., and Phillips, N. Frictional stability of Pelona–Orocopia–Rand schists under hydrothermal conditions and implications for seismic hazards in Southern California. *Earth and Planetary Science Letters*, 669:119573, Nov. 2025. doi: 10.1016/j.epsl.2025.119573.

Gvirtzman, S. and Fineberg, J. Nucleation fronts ignite the interface rupture that initiates frictional motion. *Nature Physics*, 17 (9):1037–1042, Aug. 2021. doi: 10.1038/s41567-021-01299-9.

Handin, J. On the Coulomb-Mohr failure criterion. *Journal of Geophysical Research*, 74(22):5343–5348, Oct. 1969. doi: 10.1029/jb074i022p05343.

He, C., Yao, W., Wang, Z., and Zhou, Y. Strength and stability of frictional sliding of gabbro gouge at elevated temperatures. *Tectonophysics*, 427(1–4):217–229, Dec. 2006. doi: 10.1016/j.tecto.2006.05.023.

Hertz, H. Über die Berührung fester elastischer Körper. *Journal für die reine und angewandte Mathematik*, 92:156–171, 1881.

Hirauchi, K., Yoshida, Y., Yabe, Y., and Muto, J. Slow Stick-Slip Failure in Halite Gouge Caused by Brittle-Plastic Fault Heterogeneity. *Geochemistry, Geophysics, Geosystems*, 21(9), Sept. 2020a. doi: 10.1029/2020gc009165.

Hirauchi, K.-i., Yamamoto, Y., den Hartog, S. A., and Niemeijer, A. R. The role of metasomatic alteration on frictional properties of subduction thrusts: An example from a serpentinite body in the Franciscan Complex, California. *Earth and Planetary Science Letters*, 531:115967, Feb. 2020b. doi: 10.1016/j.epsl.2019.115967.

Hobbs, D. A study of the behaviour of a broken rock under triaxial compression, and its application to mine roadways. *International Journal of Rock Mechanics and Mining Sciences & Geomechanics Abstracts*, 3(1):11–43, Mar. 1966. doi: 10.1016/0148-9062(66)90030-1.

Hobbs, D. The behavior of broken rock under triaxial compression. *International Journal of Rock Mechanics and Mining Sciences & Geomechanics Abstracts*, 7(2):125–148, Mar. 1970. doi: 10.1016/0148-9062(70)90008-2.

Horn, H. M. and Deere, D. U. Frictional Characteristics of Minerals. *Géotechnique*, 12(4):319–335, Dec. 1962. doi: 10.1680/geot.1962.12.4.319.

Hoskins, E., Jaeger, J., and Rosengren, K. A medium-scale direct friction experiment. *International Journal of Rock Mechanics and Mining Sciences & Geomechanics Abstracts*, 5(2):143–152, Mar. 1968. doi: 10.1016/0148-9062(68)90030-2.

Ikari, M. J., Saffer, D. M., and Marone, C. Effect of hydration state on the frictional properties of montmorillonite-based fault gouge. *Journal of Geophysical Research: Solid Earth*, 112(B6), June 2007. doi: 10.1029/2006jb004748.

Jaeger, J. C. The frictional properties of joints in rock. *Geofisica pura e applicata*, 43(1):148–158, May 1959. doi: 10.1007/bf01993552.

Jang, H.-S. and Jang, B.-A. New Method for Shear Strength Determination of Unfilled, Unweathered Rock Joint. *Rock Mechanics and Rock Engineering*, 48(4):1515–1534, Oct. 2014. doi: 10.1007/s00603-014-0660-3.

Jeppson, T., Lockner, D., Beeler, N., and Hickman, S. Strength Recovery in Quartzite Is Controlled by Changes in Friction in Experiments at Hydrothermal Conditions up to 200°C. *Journal of Geophysical Research: Solid Earth*, 128(5), May 2023. doi: 10.1029/2022jb025663.

Kilgore, B., Beeler, N. M., Lozos, J., and Oglesby, D. Rock friction under variable normal stress. *Journal of Geophysical Research: Solid Earth*, 122(9):7042–7075, Sept. 2017. doi: 10.1002/2017jb014049.

Kurzawski, R. M., Niemeijer, A. R., Stipp, M., Charpentier, D., Behrmann, J. H., and Spiers, C. J. Frictional Properties of Subduction Input Sediments at an Erosive Convergent Continental Margin and Related Controls on Décollement Slip Modes: The Costa Rica Seismogenesis Project. *Journal of Geophysical Research: Solid Earth*, 123(10):8385–8408, Oct. 2018. doi: 10.1029/2017jb015398.

Lilly, P. The shear behaviour of bedding planes in Mt McRae Shale with implications for rock slope design. *International Journal of Rock Mechanics and Mining Sciences & Geomechanics Abstracts*, 19(4):205–209, Aug. 1982. doi: 10.1016/0148-9062(82)90891-9.

Lu, X., Lapusta, N., and Rosakis, A. J. Pulse-like and crack-like ruptures in experiments mimicking crustal earthquakes. *Proceedings of the National Academy of Sciences*, 104(48):18931–18936, Nov. 2007. doi: 10.1073/pnas.0704268104.

Maegawa, S., Itoigawa, F., and Nakamura, T. Effect of normal load on friction coefficient for sliding contact between rough rubber surface and rigid smooth plane. *Tribology International*, 92: 335–343, Dec. 2015. doi: 10.1016/j.triboint.2015.07.014.

Maksimović, M. New description of the shear strength for rock joints. *Rock Mechanics and Rock Engineering*, 25(4):275–284, Oct. 1992. doi: 10.1007/bf01041808.

Maurer, W. C. Shear Failure of Rock Under Compression. *Society of Petroleum Engineers Journal*, 5(02):167–176, June 1965. doi: 10.2118/1054-pa.

Mehrishal, S., Sharifzadeh, M., Shahriar, K., and Song, J.-J. An Experimental Study on Normal Stress and Shear Rate Dependency of Basic Friction Coefficient in Dry and Wet Limestone Joints. *Rock Mechanics and Rock Engineering*, 49(12):4607–4629, Aug. 2016. doi: 10.1007/s00603-016-1073-2.

Mele Veedu, D., Giorgetti, C., Scuderi, M., Barbot, S., Marone, C., and Collettini, C. Bifurcations at the Stability Transition of Earthquake Faulting. *Geophysical Research Letters*, 47(19), Sept. 2020. doi: 10.1029/2020gl087985.

Mitchell, E. K., Fialko, Y., and Brown, K. M. Temperature dependence of frictional healing of Westerly granite: Experimental observations and numerical simulations. *Geochemistry, Geophysics, Geosystems*, 14(3):567–582, Mar. 2013. doi: 10.1029/2012gc004241.

Mizukami, N. and Maeno, N. Normal stress dependence of ice-ice friction coefficients. *Journal of the Japanese Society of Snow and Ice*, 62(6):515–521, 2000. doi: 10.5331/seppyo.62.515.

Moore, D. E. and Lockner, D. A. *Friction of the smectite clay montmorillonite: A review and interpretation of data*, page 317–345. Columbia University Press, Dec. 2007. doi: 10.7312/dixo13866-011.

Moore, D. E. and Lockner, D. A. Talc friction in the temperature range 25°–400° C: Relevance for Fault-Zone Weakening. *Tectonophysics*, 449(1–4):120–132, Mar. 2008. doi: 10.1016/j.tecto.2007.11.039.

Moore, D. E., Lockner, D. A., Tanaka, H., and Iwata, K. The Coefficient of Friction of Chrysotile Gouge at Seismogenic Depths. *International Geology Review*, 46(5):385–398, May 2004. doi: 10.2747/0020-6814.46.5.385.

Morrow, C. A. and Byerlee, J. D. Experimental studies of compaction and dilatancy during frictional sliding on faults containing gouge. *Journal of Structural Geology*, 11(7):815–825, Jan. 1989. doi: 10.1016/0191-8141(89)90100-4.

Morrow, C. A., Moore, D. E., and Lockner, D. A. Frictional strength of wet and dry montmorillonite. *Journal of Geophysical Research: Solid Earth*, 122(5):3392–3409, May 2017. doi: 10.1002/2016jb013658.

Murrell, S. A. F. The Effect of Triaxial Stress Systems on the Strength of Rocks at Atmospheric Temperatures. *Geophysical Journal International*, 10(3):231–281, Dec. 1965. doi: 10.1111/j.1365-246x.1965.tb03155.x.

Mutlu, O. and Bobet, A. Slip propagation along frictional discontinuities. *International Journal of Rock Mechanics and Mining Sciences*, 43(6):860–876, Sept. 2006. doi: 10.1016/j.ijrmms.2005.11.012.

Nagata, K., Nakatani, M., and Yoshida, S. Monitoring frictional strength with acoustic wave transmission. *Geophysical Research Letters*, 35(6), Mar. 2008. doi: 10.1029/2007gl033146.

Nie, S. and Barbot, S. Velocity and Temperature Dependence of Steady-State Friction of Natural Gouge Controlled by Competing Healing Mechanisms. *Geophysical Research Letters*, 51(11), June 2024. doi: 10.1029/2023gl106485.

Niemeijer, A. R., Boulton, C., Toy, V. G., Townend, J., and Sutherland, R. Large-displacement, hydrothermal frictional properties of DFDP-1 fault rocks, Alpine Fault, New Zealand: Implications for deep rupture propagation. *Journal of Geophysical Research: Solid Earth*, 121(2):624–647, Feb. 2016. doi: 10.1002/2015jb012593.

Noda, H. and Lapusta, N. Three-dimensional earthquake sequence simulations with evolving temperature and pore pressure due to shear heating: Effect of heterogeneous hydraulic diffusivity. *Journal of Geophysical Research: Solid Earth*, 115(B12), Dec. 2010. doi: 10.1029/2010jb007780.

Noda, H. and Shimamoto, T. Constitutive properties of clayey fault gouge from the Hanaore fault zone, southwest Japan. *Journal of Geophysical Research: Solid Earth*, 114(B4), Apr. 2009. doi: 10.1029/2008jb005683.

Ohnaka, M. Frictional characteristics of typical rocks. *Journal of Physics of the Earth*, 23(1):87–112, 1975. doi: 10.4294/jpe1952.23.87.

Okamoto, A. S., Verberne, B. A., Niemeijer, A. R., Takahashi, M., Shimizu, I., Ueda, T., and Spiers, C. J. Frictional Properties of Simulated Chlorite Gouge at Hydrothermal Conditions: Implications for Subduction Megathrusts. *Journal of Geophysical Research: Solid Earth*, 124(5):4545–4565, May 2019. doi: 10.1029/2018jb017205.

Okuda, H., Katayama, I., Sakuma, H., and Kawai, K. Effect of normal stress on the frictional behavior of brucite: application to slow earthquakes at the subduction plate interface in the mantle wedge. *Solid Earth*, 12(1):171–186, Jan. 2021. doi: 10.5194/se-12-171-2021.

Okuda, H., Niemeijer, A. R., Takahashi, M., Yamaguchi, A., and Spiers, C. J. Hydrothermal Friction Experiments on Simulated Basaltic Fault Gouge and Implications for Megathrust Earthquakes. *Journal of Geophysical Research: Solid Earth*, 128(1), Dec. 2022. doi: 10.1029/2022jb025072.

Orellana, L. F., Scuderi, M. M., Collettini, C., and Violay, M. Frictional Properties of Opalinus Clay: Implications for Nuclear Waste Storage. *Journal of Geophysical Research: Solid Earth*, 123(1): 157–175, Jan. 2018. doi: 10.1002/2017jb014931.

Pascoe, M. W. and Tabor, D. The friction and deformation of polymers. *Proceedings of the Royal Society of London. Series A. Mathematical and Physical Sciences*, 235(1201):210–224, Apr. 1956. doi: 10.1098/rspa.1956.0077.

Rast, M., Madonna, C., Selvadurai, P. A., Wenning, Q. C., and Ruh, J. B. Importance of Water-Clay Interactions for Fault Slip in Clay-Rich Rocks. *Journal of Geophysical Research: Solid Earth*, 129(4), Apr. 2024. doi: 10.1029/2023jb028235.

Renard, F. and Ortoleva, P. Water films at grain-grain contacts: Debye-Hückel, osmotic model of stress, salinity, and mineralogy dependence. *Geochimica et Cosmochimica Acta*, 61(10): 1963–1970, May 1997. doi: 10.1016/s0016-7037(97)00036-7.

Rice, J. R. Heating and weakening of faults during earthquake slip. *Journal of Geophysical Research: Solid Earth*, 111(B5), May 2006. doi: 10.1029/2005jb004006.

Ruggieri, R., Pozzi, G., Volpe, G., Bottazzi, F., Brignoli, M., Corradi, A. A. I., Mantica, S., Osculati, L., Petroselli, S., Volontè, G., and Collettini, C. Heterogeneous mineralogical composition and fault behaviour: A systematic study in ternary fault rock compositions. *Tectonophysics*, 891:230528, Nov. 2024. doi: 10.1016/j.tecto.2024.230528.

Saffer, D. M. and Marone, C. Comparison of smectite- and illite-rich gouge frictional properties: application to the updip limit of the seismogenic zone along subduction megathrusts. *Earth and Planetary Science Letters*, 215(1–2):219–235, Oct. 2003. doi: 10.1016/s0012-821x(03)00424-2.

Saffer, D. M., Frye, K. M., Marone, C., and Mair, K. Laboratory results indicating complex and potentially unstable frictional behavior of smectite clay. *Geophysical Research Letters*, 28(12): 2297–2300, June 2001. doi: 10.1029/2001gl012869.

Sakuma, H., Kawai, K., Katayama, I., and Suehara, S. What is the origin of macroscopic friction? *Science Advances*, 4(12), Dec. 2018. doi: 10.1126/sciadv.aav2268.

Sanei, M., Faramarzi, L., Fahimifar, A., Goli, S., Mehinrad, A., and Rahmati, A. Shear strength of discontinuities in sedimentary rock masses based on direct shear tests. *International Journal of Rock Mechanics and Mining Sciences*, 75:119–131, Apr. 2015. doi: 10.1016/j.ijrmms.2014.11.009.

Schellart, W. Shear test results for cohesion and friction coefficients for different granular materials: scaling implications for their usage in analogue modelling. *Tectonophysics*, 324(1–2): 1–16, Sept. 2000. doi: 10.1016/s0040-1951(00)00111-6.

Schulson, E. M. and Fortt, A. L. Friction of ice on ice. *Journal of Geophysical Research: Solid Earth*, 117(B12), Dec. 2012. doi: 10.1029/2012jb009219.

Segall, P. and Rice, J. R. Dilatancy, compaction, and slip instability of a fluid-infiltrated fault. *Journal of Geophysical Research: Solid Earth*, 100(B11):22155–22171, Nov. 1995. doi: 10.1029/95jb02403.

Shreedharan, S., Rivière, J., Bhattacharya, P., and Marone, C. Frictional State Evolution During Normal Stress Perturbations Probed With Ultrasonic Waves. *Journal of Geophysical Research: Solid Earth*, 124(6):5469–5491, June 2019. doi: 10.1029/2018jb016885.

Smith, S., Tesei, T., Scott, J., and Collettini, C. Reactivation of normal faults as high-angle reverse faults due to low frictional strength: Experimental data from the Moonlight Fault Zone, New Zealand. *Journal of Structural Geology*, 105:34–43, Dec.

2017. doi: 10.1016/j.jsg.2017.10.009.

Smith, S. A. F. and Faulkner, D. R. Laboratory measurements of the frictional properties of the Zuccale low-angle normal fault, Elba Island, Italy. *Journal of Geophysical Research: Solid Earth*, 115 (B2), Feb. 2010. doi: 10.1029/2008jb006274.

Sone, H., Shimamoto, T., and Moore, D. E. Frictional properties of saponite-rich gouge from a serpentinite-bearing fault zone along the Gokasho-Arashima Tectonic Line, central Japan. *Journal of Structural Geology*, 38:172–182, May 2012. doi: 10.1016/j.jsg.2011.09.007.

Sulem, J. and Famin, V. Thermal decomposition of carbonates in fault zones: Slip-weakening and temperature-limiting effects. *Journal of Geophysical Research: Solid Earth*, 114(B3), Mar. 2009. doi: 10.1029/2008jb006004.

Takahashi, M., Mizoguchi, K., and Masuda, K. Potential of phyllosilicate dehydration and dehydroxylation reactions to trigger earthquakes. *Journal of Geophysical Research: Solid Earth*, 114 (B2), Feb. 2009. doi: 10.1029/2008jb005630.

Tesei, T., Harbord, C. W. A., De Paola, N., Collettini, C., and Viti, C. Friction of Mineralogically Controlled Serpentinites and Implications for Fault Weakness. *Journal of Geophysical Research: Solid Earth*, 123(8):6976–6991, Aug. 2018. doi: 10.1029/2018jb016058.

Thomas, A. M., Watkins, J. M., Beeler, N., French, M. E., Behr, W. M., and Reed, M. H. Rapid fault healing from cementation controls the dynamics of deep slow slip and tremor. *Science Advances*, 11(47), Nov. 2025. doi: 10.1126/sciadv.adz2832.

Veedu, D. M. and Barbot, S. The Parkfield tremors reveal slow and fast ruptures on the same asperity. *Nature*, 532(7599):361–365, Apr. 2016. doi: 10.1038/nature17190.

Viesca, R. C. and Garagash, D. I. Ubiquitous weakening of faults due to thermal pressurization. *Nature Geoscience*, 8(11):875–879, Oct. 2015. doi: 10.1038/ngeo2554.

Volpe, G., Affinito, R., Calzolari, L., Pozzi, G., Marone, C., and Collettini, C. The influence of cementation on fault stability. *Earth and Planetary Science Letters*, 671:119674, Dec. 2025. doi: 10.1016/j.epsl.2025.119674.

Volpe, G., Affinito, R., Calzolari, L., Pozzi, G., Marone, C., and Collettini, C. Reply to the comment on "The influence of cementation on fault stability". *Earth and Planetary Science Letters*, 679: 119867, Apr. 2026. doi: 10.1016/j.epsl.2026.119867.

Wang, L. and Barbot, S. Excitation of San Andreas tremors by thermal instabilities below the seismogenic zone. *Science Advances*, 6(36), Sept. 2020. doi: 10.1126/sciadv.abb2057.

Wu, B. and Barbot, S. Evolution of the real area of contact during laboratory earthquakes. *Proceedings of the National Academy of Sciences*, 122(23), June 2025. doi: 10.1073/pnas.2410496122.

Yamashita, F., Fukuyama, E., and Mizoguchi, K. Probing the slip-weakening mechanism of earthquakes with electrical conductivity: Rapid transition from asperity contact to gouge comminution. *Geophysical Research Letters*, 41(2):341–347, Jan. 2014. doi: 10.1002/2013gl058671.

Yashima, S., Romero, V., Wandersman, E., Frétigny, C., Chaudhury, M. K., Chateauminois, A., and Prevost, A. M. Normal contact and friction of rubber with model randomly rough surfaces. *Soft Matter*, 11(5):871–881, 2015. doi: 10.1039/c4sm02346c.

Zhang, L. and He, C. Frictional properties of phyllosilicate-rich mylonite and conditions for the brittle-ductile transition. *Journal of Geophysical Research: Solid Earth*, 121(4):3017–3047, Apr. 2016. doi: 10.1002/2015jb012489.

Zhang, L., He, C., Liu, Y., and Lin, J. Frictional properties of the South China Sea oceanic basalt and implications for strength of the Manila subduction seismogenic zone. *Marine Geology*, 394: 16–29, Dec. 2017. doi: 10.1016/j.margeo.2017.05.006.